

Formation of black holes in the pair-instability mass gap: Hydrodynamical simulation of a massive star collision

Alessandro Ballone,^{1,2,3}★ Guglielmo Costa,^{1,2,3} Michela Mapelli,^{1,2,3}† Morgan MacLeod⁴

¹Physics and Astronomy Department Galileo Galilei, University of Padova, Vicolo dell'Osservatorio 3, I-35122 Padova, Italy

²INAF - Osservatorio Astronomico di Padova, Vicolo dell'Osservatorio 5, I-35122 Padova, Italy

³INFN - Padova, Via Marzolo 8, I-35131 Padova, Italy

⁴Center for Astrophysics | Harvard & Smithsonian 60 Garden Street, MS-16, Cambridge, MA 02138, USA

Accepted XXX. Received YYY; in original form ZZZ

ABSTRACT

The detection of GW190521 by the LIGO-Virgo collaboration proved the existence of black holes in the theoretically predicted pair-instability gap of their mass spectrum. Some recent studies suggest that such massive black holes could be produced by the collision of an evolved star with a carbon-oxygen core and a main sequence star. Such a post-coalescence star could end its life avoiding the pair-instability regime and with a direct collapse of its very massive envelope. It is still not clear, however, how the collision shapes the structure of the newly produced star and how much mass is actually lost in the impact. We investigated this issue by means of hydrodynamical simulations with the smoothed particle hydrodynamics code *STARSMASHER*, finding that the collision can remove up to 12% of the initial mass of the colliding stars. This is a non-negligible percentage of the initial mass and could affect the further evolution of the stellar remnant, particularly in terms of the final mass of a possibly forming black hole, if the core avoids the pair-instability regime. We also found that the main sequence star can plunge down to the outer boundary of the carbon-oxygen core of the primary, changing the inner chemical composition of the remnant. The collision expels the outer layers of the primary, leaving a remnant with an helium-enriched envelope (reaching He fractions of about 0.4 at the surface). These more complex abundance profiles can be directly used in stellar evolution simulations of the collision product.

Key words: stars: massive – stars: evolution – stars: peculiar – hydrodynamics – black hole physics

1 INTRODUCTION

Stellar evolution models predict a gap in the mass spectrum of black holes between ~ 60 and $\sim 120 M_{\odot}$ (the so-called “pair instability mass gap”; e.g., Heger & Woosley 2002; Woosley et al. 2007; Belczynski et al. 2016; Spera & Mapelli 2017; Woosley 2017; Stevenson et al. 2019; Marchant et al. 2019; Farmer et al. 2019; Leung et al. 2019; Marchant et al. 2019; Marchant & Moriya 2020; Renzo et al. 2020a; Tanikawa et al. 2021). Pair instability affects those massive stars that develop carbon-oxygen (CO) cores with densities between $\approx 10^2 - 10^6 \text{ g cm}^{-3}$ and temperatures above $6 \times 10^8 \text{ K}$. For these physical conditions, thermal energy is converted into mass of electron-positron pairs. Depending on the CO core mass, this sudden lack of thermal support can lead to cyclic phases of hydrodynamical instability of the star that can result into strong mass loss (pulsational pair-instability) or even to a single hydrodynamical instability phase that leads to the total collapse of the star and completely destroys it (pair-instability supernova).

Gravitational-wave observations seem to challenge the existence of such gap. During the third observing run, the LIGO-Virgo collaboration detected a black hole merger event, GW190521, with primary and secondary mass 85^{+21}_{-14} and $66^{+17}_{-18} M_{\odot}$, respectively

(Abbott et al. 2020a,b). The mass of the primary black hole of GW190521 lies within the predicted mass gap, while the mass of the secondary is close to its lower boundary. Furthermore, three additional gravitational-wave event candidates might be associated with black holes in the mass gap: GW190403_051519, GW190426_190642 (Abbott et al. 2021a) and GW200220_061928 (Abbott et al. 2021b). Finally, Nitz et al. (2021) recently reported another potential event candidate with primary mass overlapping with the mass gap (GW200129_114245).

Our knowledge of the boundaries of the pair-instability mass gap is hampered by several uncertainties about massive stellar evolution: recent work has shown that the gap might be substantially shorter than initially predicted (e.g., Croon et al. 2020; Farmer et al. 2020; Costa et al. 2021; Woosley & Heger 2021). Alternatively, GW190521 might be a 2nd generation black hole merger, in which the primary and maybe also the secondary black hole are the result of a previous merger. Such hierarchical mergers are shown to be occurring in star clusters (Miller & Hamilton 2002; Gerosa & Berti 2017; Fishbach et al. 2017; Rodriguez et al. 2019; Antonini et al. 2019; Fragione et al. 2020; Rodriguez et al. 2020; Mapelli et al. 2022, 2021) or triggered by massive gaseous disks in active galactic nuclei (e.g., McKernan et al. 2012, 2018; Bartos et al. 2017; Stone et al. 2017; Yang et al. 2019; Tagawa et al. 2020, 2021).

Finally, stellar collisions provide an additional pathway for the formation of black holes in the pair-instability gap (Di Carlo et al. 2019,

★ E-mail: ale.ballone@gmail.com

† E-mail: michela.mapelli@unipd.it

2020a,b; Spera et al. 2019; Kremer et al. 2020; Rastello et al. 2021). Simulations of young massive star clusters show that dynamical encounters efficiently trigger collisions between massive stars. If an evolved star with a relatively low-mass core collides with a massive star in its main sequence, the product of such collision could consist of a star with the same core, but with a much more massive envelope. This exotic star can, in principle, avoid the pair-instability phase and eventually evolve until it directly collapses into a black hole with mass comparable to the sum of the masses of the two colliding stars (Di Carlo et al. 2019, 2020a,b).

Renzo et al. (2020b) focused on a specific stellar collision described in Di Carlo et al. (2020b), involving a core helium burning star of $\approx 58 M_{\odot}$ and a main sequence star of $\approx 42 M_{\odot}$. In their study, they used the stellar evolution code MESA (Paxton et al. 2011, 2019) to compute the stellar structures of both stars for a time equal to the end of the main sequence of the most massive star. Then, they relaxed the primary star by adding the mass of the secondary to its envelope (hence reaching a total mass of $\approx 100 M_{\odot}$) and assuming that the envelope of the primary is enriched - uniformly with radius - with He brought by the H-burning core of the secondary. In this way, Renzo et al. (2020b) found that this system can directly collapse into a black hole in the pair-instability mass gap.

One of the main uncertainties of the approach of Di Carlo et al. (2020b) and Renzo et al. (2020b) is in how the collision actually shapes the collision product, both in terms of mass unbound and in terms of chemical enrichment of the primary's envelope. While a certain number of hydrodynamical simulations of stellar collisions have been carried out (for head-on or low impact-parameter collisions, see Lombardi et al. 1996; Sills et al. 2001; Lombardi et al. 2002; Gaburov et al. 2010b; Glebbeek et al. 2013), very few involve extremely massive stars in their post main sequence phase, as those possibly leading to black holes in the pair-instability gap.

In this work, we simulate the collision of two massive stars (similar to the ones considered by Di Carlo et al. 2020b and Renzo et al. 2020b), and study the structure of the collision product, by means three-dimensional hydrodynamical simulations. We find that up to $\sim 12\%$ of the initial mass is lost during the collision, and quantify the chemical mixing in the post-coalescence product.

2 METHODS

To investigate how the collision shapes the structure of the final star, we ran simulations with the smoothed-particle hydrodynamics (SPH) code STARSMASHER¹ (Gaburov et al. 2010b), which is particularly suited to model stellar collisions. In its last version, the code implements variational equations of motion and libraries to calculate the gravitational forces between particles using direct summation on NVIDIA GPUs (Gaburov et al. 2010a). Using a direct summation instead of a tree-based algorithm for gravity increases the accuracy of the gravity calculations, particularly in terms of energy and angular momentum conservation. At the end of our simulation, the total energy was conserved within a factor 1.5×10^{-5} . The thermodynamical treatment of STARSMASHER is simplified, compared to the one of sophisticated stellar evolution codes, and is based on a simple polytropic equation of state with adiabatic index $\gamma = 5/3$ (Rasio & Shapiro 1995), including the contribution of radiation pressure (Lombardi et al. 2006). To generate initial conditions, STARSMASHER

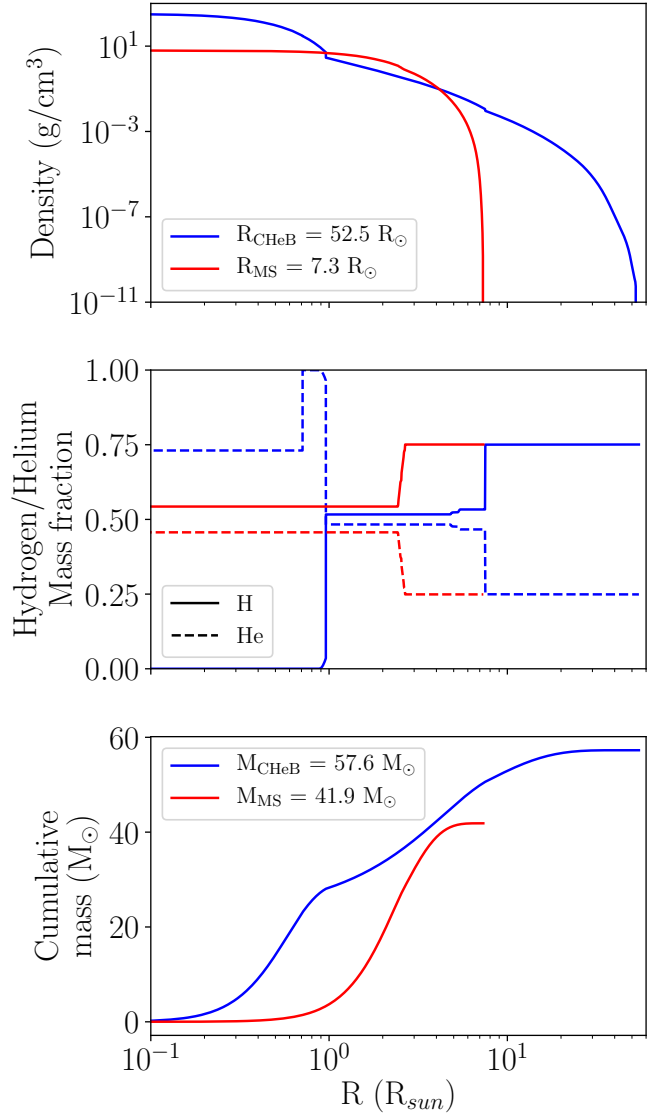


Figure 1. Density (upper panel), hydrogen and helium mass fraction (middle panel: H, solid line; He, dashed line) and cumulative mass profiles (lower panel) for the CHeB (blue) and MS star (red), for our initial conditions.

comes with an internal module to initialize stars from tables containing one-dimensional profiles of their main properties.

In the dynamical simulations of Di Carlo et al. (2020b), a black hole of $88 M_{\odot}$ is produced by the remnant of the collision between two massive stars, namely:

- a core helium burning (CHeB) star, with mass $M_{\text{CHeB}} = 57.6 M_{\odot}$.
- a main sequence (MS) star, with mass $M_{\text{MS}} = 41.9 M_{\odot}$.

These two stars were members of a binary system and collided with each other as the result of a binary-single interaction, in which a perturber brought the two stars into a nearly-radial orbit. Both stars have metallicity $Z = 0.0002 \sim 0.01 Z_{\odot}$. As visible in Figure 1, we chose a CHeB primary which has a well developed core, in which part of the helium has already been converted into carbon and oxygen.

¹ <https://github.com/jalombard/starasmasher/>.

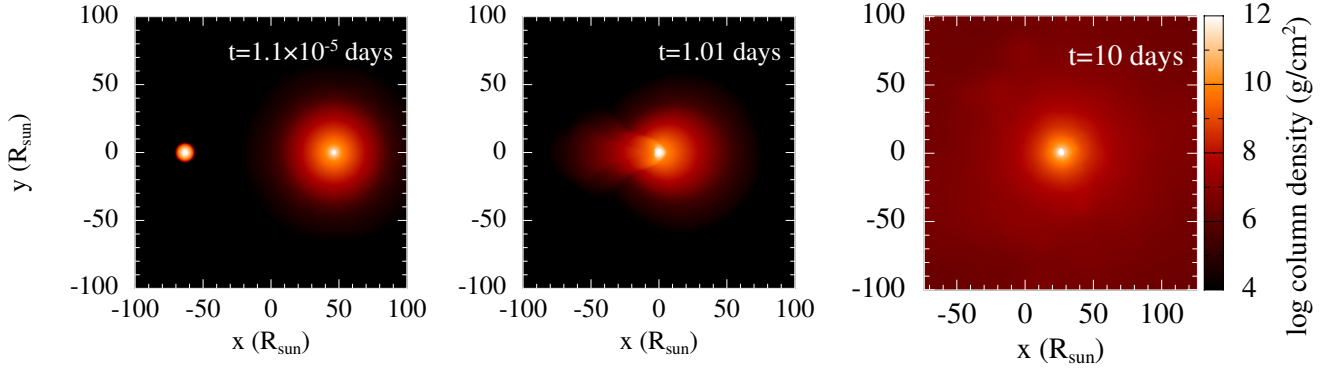


Figure 2. Column mass density maps for our hydrodynamical simulation, at the beginning (left-hand panel), at the time of the collision (central panel) and at the end of the simulation (i.e., after 10 days of evolution; right-hand panel).

The structure of our primary star is significantly different from the one considered by [Renzo et al. \(2020b\)](#), who assumed a primary star at the end of its MS, that is with a negligible fraction of CO in the core.

To generate the initial conditions for *STARSMASHER*, we create the one-dimensional profiles of these two stars using the stellar evolution code *PARSEC* ([Bressan et al. 2012; Costa et al. 2019](#)). Details about the *PARSEC* setup used for these simulations can be found in a companion paper ([Costa et al. 2022](#)). Figure 1 shows the density (upper panel), H and He abundance (middle panel) and cumulative mass (lower panel) profiles of the two stars. *STARSMASHER* re-samples these one-dimensional profiles with SPH particles distributed in the three-dimensional space, by keeping the number density of particles uniform. This feature is particularly important, since the mass density of stars spans several orders of magnitude from their center to their atmospheres (Fig. 1). In this way, particles with different masses can spatially sample each layer of the star in a uniform way. We chose to sample the CHeB and MS star with 8×10^5 and 9×10^4 particles, respectively. Such big difference in resolution is forced by the much wider dynamical range of mass density spanned by the CHeB star and by its much larger radius. As a result, the mass resolution of SPH particles ranges from $\approx 2 \times 10^{-11}$ to $\approx 7.6 M_\odot$ and from $\approx 4 \times 10^{-7}$ to $1.4 \times 10^{-2} M_\odot$ for the CHeB and MS star, respectively.

When importing the stellar profiles, *STARSMASHER* checks whether the central density is four times higher than the average density of the stars; in that case, it sets a central core particle. For this reason, the core of our CHeB star is sampled by a central non-gravitating core particle with mass equal to $7.6 M_\odot$ and smoothing length equal to $1 R_\odot$ and six SPH particles surrounding it (at about $0.35 R_\odot$) with mass of about $3.5 M_\odot$ and smoothing length equal to $0.9 R_\odot$. Setting these large smoothing lengths (of the order of the core size) avoids spurious numerical effects due to gravitational perturbation of the surroundings by these central massive particles. Furthermore, while not being well sampled spatially, most of the mass of the core is sampled by these six massive SPH particles, which thermal pressure prevents outer particles from spuriously penetrating the core.

Before initializing the collision simulation, the two stars were evolved singularly in relaxation runs, to allow the SPH particles to re-adjust to equilibrium (for more details, see [Gaburov et al. 2010b](#)), because of the spatial resolution and the slightly different equation of state implemented in *STARSMASHER* with respect to *PARSEC* stellar evolution model.

After these preliminary steps, we put the two stars on a hyperbolic radial orbit, with velocity at infinity $v_\infty = 10 \text{ km s}^{-1}$ and initial

separation of $d_{\text{init}} = 110 R_\odot \gtrsim 2 R_{\text{CHeB}}$, where $R_{\text{CHeB}} = 52.5 R_\odot$ is the radius of the CHeB star. Our choice of v_∞ matches the velocity dispersion in young massive star clusters, such as those simulated by [Di Carlo et al. \(2020b\)](#). Nonetheless, the value of v_∞ adopted here is much lower than $\sqrt{2G(M_{\text{CHeB}} + M_{\text{MS}})/d_{\text{init}}} \approx 600 \text{ km s}^{-1}$, so it has very little impact on the collision. We assumed an impact parameter equal to zero because we wanted to probe the most extreme case in terms of kinetic energy of the collision and to obtain an upper limit to the mass loss. In a follow-up study ([Ballone et al.](#), in preparation) we will explore different configurations.

While the total permeation of the two stars occurs in about 1 day of simulated time, we decided to evolve our model for 10 days, to allow as much hydrodynamic relaxation of the collision product as possible. This timescale is sufficient to reach hydro-static equilibrium. The thermal relaxation of the new star occurs over a much longer time, that is several times the Kelvin-Helmholtz timescale of the remnant, and is best treated by one-dimensional stellar evolution codes ([Costa et al. 2022](#)).

3 RESULTS

Figure 2 shows the evolution of the collision at the beginning of the simulation, during the maximum permeation of the two stars and at the end of the simulation. As visible in the central panel, as the MS star plunges in the atmosphere of the CHeB star, its outer layers form a strong shock in the frontal side of the collision, while they lead to a cometary tail in the back side. When the MS star reaches a separation, relative to the core of the CHeB star, of the order of its Roche limit (i.e., about the star’s initial radius, in the simple Roche approximation), it is tidally disrupted by the core of the CHeB star. After the coalescence, the remnant star shows a much more extended envelope, generated by the inflation of the outer layers of the primary star due to conversion of the kinetic energy of the impact into thermal and kinetic energy of those layers.

Figure 3 shows density, H and He abundances, pressure, temperature and cumulative mass profiles for the stellar remnant, obtained through a mass-weighted average of these quantities over spherical shells centered on the core of the final star. In order to calculate these profiles, we estimated which particles are still bound to the remnant, with a simplified approach. For each i -th SPH particle, we calculated

$$e_i = v_{\text{cm},i}^2 + u_i - GM_{\text{encl},i}/d_{\text{cm},i}, \quad (1)$$

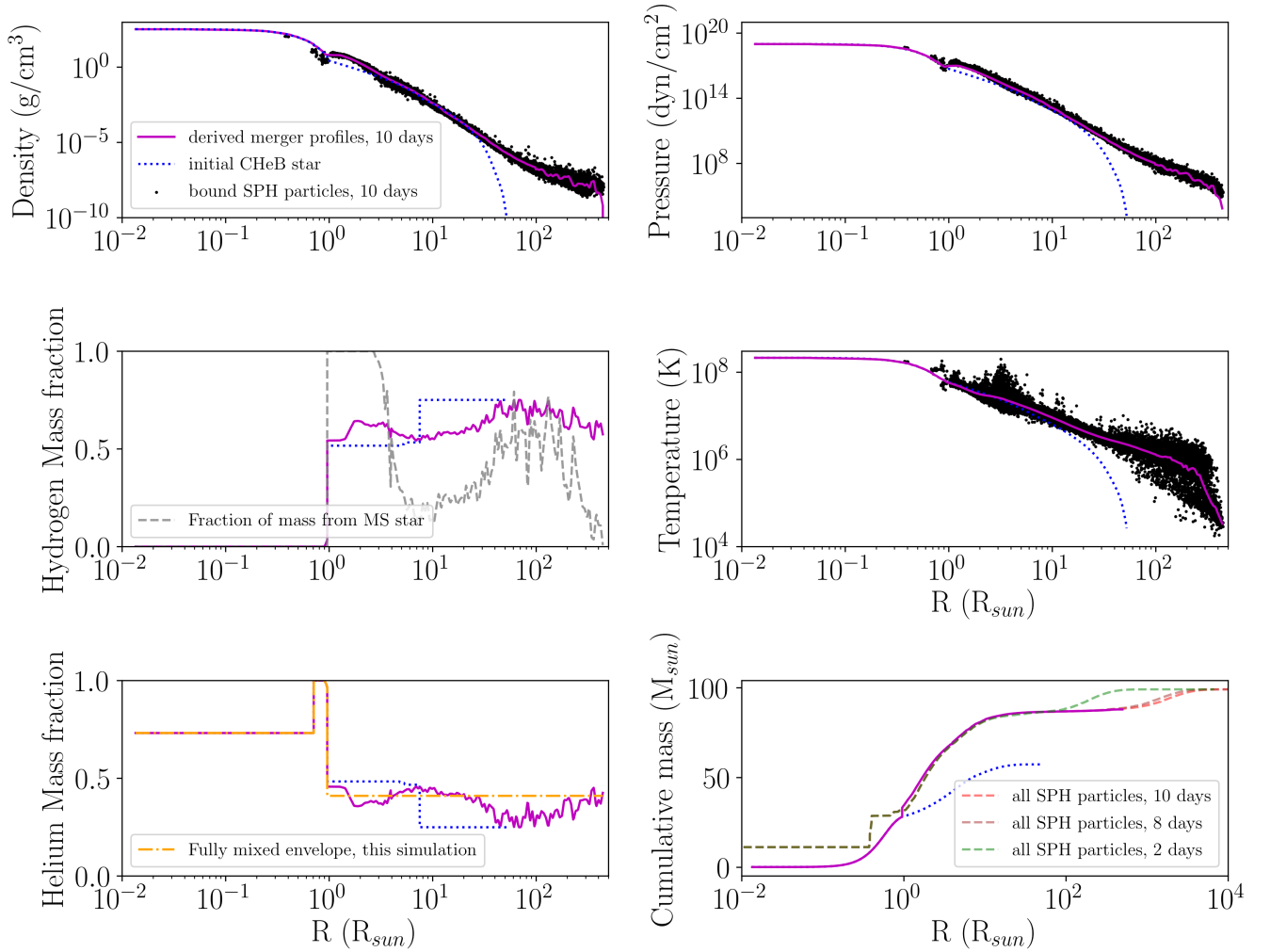


Figure 3. Density (upper left), hydrogen (middle left) and helium (lower left) mass fractions, pressure (upper right), temperature (middle right) and cumulative mass (lower right) profiles for the post-collision star at the end of the simulation (10 days; solid magenta lines). We consider only SPH particles that are still bound to the remnant (black dots, see eq. 1 for details). As a comparison, we also show the original profiles for the CHEB star (blue dotted line). In the middle left-hand panel we also plot the fraction of mass, in each bin, coming from the original MS star (gray dashed line). In the lower left-hand panel we also show the He abundance for a fully mixed envelope (see text). Finally, for the cumulative mass panel, we also compare the obtained profile to the cumulative mass profile of all the SPH particles (bound+unbound) at a simulation time of 2 (green dashed line), 8 (brown dashed line) and 10 days (red dashed line).

where e_i and u_i are the specific total and internal energy, $v_{\text{cm},i}$ and $d_{\text{cm},i}$ are the velocity and distance calculated with respect to the total center of mass, and $M_{\text{encl},i}$ is the total mass enclosed within $d_{\text{cm},i}$. Every particle with positive e_i is considered unbound and is excluded from the calculation of the remnant profiles. We assumed that the core of the remnant has exactly the same properties as the core of the original CHEB star, hence the profiles in the inner $1 R_\odot$ are just taken from the initial PARSEC profiles of the primary, used to initialize our simulation.

As visible particularly in the cumulative mass profiles (lower right-hand panel of Fig. 3), the SPH particles re-adjust to a new mass distribution that is more concentrated compared to the one of the initial CHEB star, but that extends up to a much larger radius of

$\approx 450 R_\odot$. The lower right-hand panel also shows that the unbound mass is in a large bulk of particles that are launched at much larger radii ($> 1000 R_\odot$) already 8 days after the collision.

From this calculation, we got that the mass of the collision product is $\approx 87.9 M_\odot$, i.e. about 11.7% of the initial stellar mass is lost in the impact. In particular, the final star retains about 82% and 98% of the mass of the CHEB star and MS star, respectively. Hence, the structure of the CHEB expands in the collision, with its shock-heated outer envelope ending up unbound.

In order to calculate abundances profiles, we assigned each particle at the beginning of the simulation the hydrogen and helium mass fractions of the shell of the original stars they initially belonged to. In this way, chemical abundances are simply advected by the

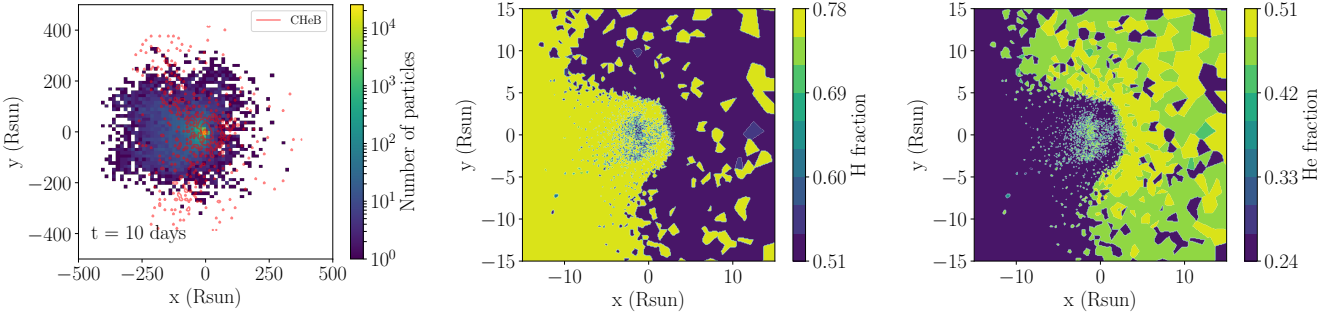


Figure 4. Left-hand panel: x - y projected distribution of SPH particles from the original CHeB (red contours) and MS (2-dimensional histogram) stars. Middle panel: Voronoi tessellation map of the particle hydrogen mass fraction, projected in the x - y domain. Right-hand panel: same as for the middle panel, but for the helium mass fraction. All panels refer to the end of our simulation, i.e., $t = 10$ days.

SPH particles, in a Lagrangian fashion. The post-collision abundance profiles show that:

- the MS star disrupts outside the denser core of the CHeB star, depositing most of its material in a shell surrounding the core ($1 R_{\odot} \lesssim d_{cm} \lesssim 5 R_{\odot}$), enriching this region with hydrogen;
- some ram-pressure stripped and shocked outer layers of the MS star are deposited further out in the envelope. As a result, at larger distances from the center ($d_{cm} \gtrsim 5 R_{\odot}$), the profile shows an increase in H, with a maximum H-enrichment at about $100 R_{\odot}$ (similar to the original radius of the CHeB envelope);
- the collision expels part of the envelope of the CHeB star and the outer layers of the remnant are mostly composed of material originally belonging to the H-burning shell of the CHeB star.

In particular, the abundance profiles surrounding the core of the remnant almost perfectly match those of the original MS star (Fig. 1). This happens because the shell between 1 and $5 R_{\odot}$ is totally composed of material originally belonging to the MS star (gray dashed line in the central left-hand panel of Fig. 3). With a similar argument, the He at large radii is material belonging to the He-shell of the original CHeB star that is brought at larger radii by the impact. The MS star pollutes the outer envelope mostly between 40 and $200 R_{\odot}$, leading to the dip in He abundance in that region and leaving higher He fractions in the outer $\approx 300 R_{\odot}$ of the newly formed star.

For comparison, were we assuming a complete mixing of the MS with the CHeB original envelope, we would have obtained a constant He fraction in the envelope of the new star equal to 0.41 (orange dashed-dotted line in the lower left panel of Fig. 3). This is a lower He fraction than assumed by Renzo et al. (2020b), due to the different structure of the two initial stars (see Sec. 2). A somewhat exotic He fraction in the envelope would imply a different position of the stellar remnant in the Hertzsprung-Russell diagram and peculiar line absorption features of its spectrum.

By looking at the three-dimensional distributions, our simulation shows that significant asymmetries arise in the spatial profile and chemical composition (Fig. 4). Especially at large radii, particles originally belonging to the MS star are distributed along the radial stellar orbit, with the shape of a cometary tail. This Figure also clearly shows that the fresh hydrogen brought in the envelope of the post-coalescence star is mostly one-sided, except for the closest vicinity to the original CHeB core. We report spherically-averaged quantities in Fig. 3, because we expect any rotation imparted by a non-zero impact parameter to azimuthally redistribute this material.

4 DISCUSSION

Our simulation shows that up to 12% of the CHeB star's envelope mass can be lost in a collision similar to the one described in Di Carlo et al. (2020b). Our assumption of a head-on collision must be regarded as an upper limit to the mass loss.

Our result is in agreement with the relation obtained by Lombardi et al. (2002); according to their findings, the fraction f of mass loss in our head-on collisions should be

$$f = c_1 \frac{q}{(1+q)^2} \frac{R_{\text{CHeB},0.86} + R_{\text{MS},0.86}}{R_{\text{CHeB},0.5} + R_{\text{MS},0.5}}, \quad (2)$$

where $c_1 = 0.157$, $q = M_{\text{MS}}/M_{\text{CHeB}}$ and $R_{\text{CHeB},0.86} \approx 6.64 R_{\odot}$ ($R_{\text{CHeB},0.5} \approx 1.06 R_{\odot}$) and $R_{\text{MS},0.86} \approx 3.47 R_{\odot}$ ($R_{\text{MS},0.5} \approx 2.15 R_{\odot}$) are the radii of the CHeB and MS stars containing the 86% (50%) of their total mass. When applying this formula to our initial conditions, we found that the predicted mass lost is 12%.

We can also compare our simulation to an approximation that is frequently used in the literature to derive the structure of stars formed in gentle (i.e., shock-free) mergers (see, e.g., Gaburov et al. 2008; Glebbeek et al. 2013), where the post-collision particles are assumed to arrange radially with increasing initial specific entropy. Before and after the collision, we calculate the entropic variable (or buoyancy), A , of each particle, defined as (Gaburov et al. 2008)

$$A = \frac{P_{\text{tot}}}{\rho^{5/3}} \exp [8(1-\beta)/\beta], \quad (3)$$

where $P_{\text{tot}} = P_{\text{gas}} + P_{\text{rad}}$ is the total pressure, including both the gas and the black-body radiation pressure, ρ is the gas density and $\beta = P_{\text{gas}}/P_{\text{tot}}$. In one-dimensional hydro-static equilibrium, A will monotonically increase outward.

Figure 5 compares the initial to post-collision profiles of A with cumulative mass. Sorting the particles of the initial colliding stars by increasing A predicts that the MS star would sink down to the outer boundary of the CHeB core even in the case of a less extreme collision, with non-zero impact parameter. This is also in good agreement with the conditions at the end of our simulation, which are also plotted in Figure 5. A large portion of the MS star sinks to near the core of CHeB star with relatively small changes in A , indicating that much of the MS material is not strongly affected by shocks in the plunge. The entropy sorting also confirms that the core of the primary star is not penetrated by the secondary in the collision, because of its lower specific entropy. As already discussed in the literature (e.g., case P in Glebbeek & Pols 2008; Glebbeek et al. 2013), when the primary star is in a sufficiently late stage of its evolution, its core becomes the core of the collision product.

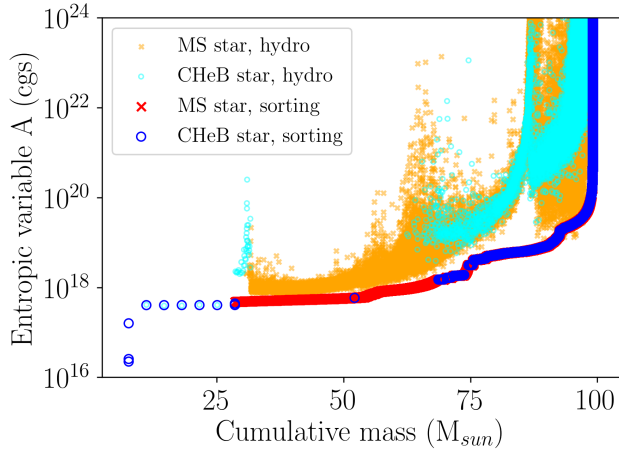


Figure 5. Entropic variable A as a function of cumulative mass, for our initial conditions sorted by increasing value of A (blue and red large circles for the CHeB and MS star, respectively) and for the output of our hydrodynamical simulation (cyan and orange small circles for the CHeB and MS star, respectively).

However, traces of shocked material that significantly modify the initial entropy profile are also present in Figure 5. These are especially clearly seen in the specific entropy of the outer $\sim 25 M_{\odot}$, and the distribution of shock-heated and ablated MS material within those outer layers. This shock-heating has the effect of rearranging the post-collision structure relative to what might be predicted by the initial entropy sorting (in one extreme) or completely homogeneous mixing (in the other extreme). Thus, the details of the shock-heating in the collision process are crucial in shaping the final post-coalescence composition shown in Figure 2.

We conclude, independently of our zero-impact parameter orbital configuration, that the envelope of the primary star can be strongly enriched by material of the secondary (in our case, a large amount of fresh hydrogen) in the vicinity of the CHeB core. Physically, this arises because of the density and specific entropy contrast between the MS star and the CHeB envelope. In their post-collision model, Renzo et al. (2020b) assume that the MS star mixes with the envelope of the more evolved star homogeneously with radius, with a uniform He fraction of 0.52 in the envelope of the collision product². Our simulation instead predicts a variable H/He abundance depending on the distance from the central core.

The expelled mass largely originates into the outer, H-rich envelope of the CHeB star. As a consequence, the outer envelope of the stellar remnant has higher He abundances compared to those of the outer layers of the original CHeB star, reaching values of the order of 0.4 at the surface.

In a companion paper (Costa et al. 2022), we carefully model the evolution of a star with same mass and chemical abundance profiles of our model, confirming that it can collapse to a black hole directly, though the final mass of the black hole is sensitive to the fraction of the envelope that can be ejected during a failed supernova (e.g., Fernández et al. 2018).

As a possible caveat, a larger impact parameter could reduce the

amount of mass lost in the impact and would induce differential rotation in the collision product (e.g., Rasio & Shapiro 1995; Sills et al. 2001; Schneider et al. 2019). This could lead to higher mixing in the envelope and have some impact on the evolution of the remnant. The initial velocity at infinity represents another important assumption: here, we chose $v_{\infty} = 10 \text{ km s}^{-1}$ to mimic collisions in young stellar clusters. Encounters in more massive star clusters (e.g., nuclear star clusters) involve higher relative velocities ($\approx 50 - 100 \text{ km s}^{-1}$). Furthermore, we also expect our results to significantly depend on the evolutionary phase of the two colliding stars. In a follow-up study, we will address these uncertainties, by running a large grid of hydrodynamical simulations with a range of impact parameters, relative velocities, and evolutionary phases.

5 SUMMARY

We modeled the collision between a primary massive CHeB star and a secondary massive MS star, by means of a detailed hydrodynamical simulation. This kind of collisions leads to a very massive star with a relatively small core and an oversized envelope. As already discussed in Di Carlo et al. (2020a) and Renzo et al. (2020b), these exotic stars might form black holes in the pair-instability mass gap.

With our work, we showed that even in the case of a head-on collision, our stellar remnant has a mass of $\approx 88 M_{\odot}$. The mass lost during the collision is 12% of the initial total mass of the two stars, and is mostly part of the H-rich outer envelope of the CHeB star.

Our model also shows that the MS star is expected to plunge down to the outer boundary of the CHeB core, hence completely rearranging the chemical composition of the post-coalescence star. The collision product shows large He abundances at its surface (≈ 0.4 for our model), which are a very distinctive observational feature.

Our results confirm that stellar collisions are a viable mechanism to form black holes in the mass gap ($\sim 60 - 120 M_{\odot}$), even if the details depend on the late evolution of the stellar remnant (Costa et al. 2022) and on the mass fraction that can be ejected during a failed supernova (e.g., Fernández et al. 2018).

ACKNOWLEDGEMENTS

AB, GC and MM acknowledge financial support by the European Research Council for the ERC Consolidator grant DEMOBLACK, under contract no. 770017. We acknowledge the CINECA award HP10CCQZCO under the ISCRA initiative and the CINECA-INFN agreement, for the availability of high performance computing resources and support. M. MacLeod acknowledges support by the US National Science Foundation under Grant No. 1909203. The initial conditions were obtained with the stellar evolution code PARSEC (Bressan et al. 2012; Costa et al. 2019) and the hydrodynamical simulations were run with the SPH code STARSMAHER (Gaburov et al. 2010b). The figures and the data analysis were performed either through the free and open source visualisation tool SPLASH (Price 2007) or through PYTHON's libraries NUMPY and MATPLOTLIB.

DATA AVAILABILITY

The data underlying this article will be shared on reasonable request to the corresponding authors.

² This specific value depends on the specific choice of the properties of the colliding MS star.

REFERENCES

- Abbott R., et al., 2020a, *Phys. Rev. Lett.*, **125**, 101102
- Abbott R., et al., 2020b, *ApJ*, **900**, L13
- Abbott R., et al., 2021a, arXiv e-prints, p. [arXiv:2108.01045](#)
- Abbott R., et al., 2021b, arXiv e-prints, p. [arXiv:2111.03606](#)
- Antonini F., Gieles M., Gualandris A., 2019, *MNRAS*, **486**, 5008
- Bartos I., Kocsis B., Haiman Z., Márka S., 2017, *ApJ*, **835**, 165
- Belczynski K., et al., 2016, *A&A*, **594**, A97
- Bressan A., Marigo P., Girardi L., Salasnich B., Dal Cero C., Rubele S., Nanni A., 2012, *MNRAS*, **427**, 127
- Costa G., Girardi L., Bressan A., Marigo P., Rodrigues T. S., Chen Y., Lanza A., Goudfrooij P., 2019, *MNRAS*, **485**, 4641
- Costa G., Bressan A., Mapelli M., Marigo P., Iorio G., Spera M., 2021, *MNRAS*, **501**, 4514
- Costa G., Ballone A., Mapelli M., Bressan A., 2022, arXiv e-prints, p. [arXiv:2204.03492](#)
- Croon D., McDermott S. D., Sakstein J., 2020, arXiv e-prints, p. [arXiv:2007.07889](#)
- Di Carlo U. N., Giacobbo N., Mapelli M., Pasquato M., Spera M., Wang L., Haardt F., 2019, *MNRAS*, **487**, 2947
- Di Carlo U. N., Mapelli M., Bouffanais Y., Giacobbo N., Santoliquido F., Bressan A., Spera M., Haardt F., 2020a, *MNRAS*, **497**, 1043
- Di Carlo U. N., et al., 2020b, *MNRAS*, **498**, 495
- Farmer R., Renzo M., de Mink S. E., Marchant P., Justham S., 2019, *ApJ*, **887**, 53
- Farmer R., Renzo M., de Mink S. E., Fishbach M., Justham S., 2020, *ApJ*, **902**, L36
- Fernández R., Quataert E., Kashiyama K., Coughlin E. R., 2018, *MNRAS*, **476**, 2366
- Fishbach M., Holz D. E., Farr B., 2017, *ApJ*, **840**, L24
- Fragione G., Loeb A., Rasio F. A., 2020, *ApJ*, **902**, L26
- Gaburov E., Lombardi J. C., Portegies Zwart S., 2008, *MNRAS*, **383**, L5
- Gaburov E., Bédorf J., Portegies Zwart S., 2010a, OCTGRAV: Sparse Octree Gravitational N-body Code on Graphics Processing Units (ascl:1010.048)
- Gaburov E., Lombardi James C. J., Portegies Zwart S., 2010b, *MNRAS*, **402**, 105
- Gerosa D., Berti E., 2017, *Phys. Rev. D*, **95**, 124046
- Glebbeek E., Pols O. R., 2008, *A&A*, **488**, 1017
- Glebbeek E., Gaburov E., Portegies Zwart S., Pols O. R., 2013, *MNRAS*, **434**, 3497
- Heger A., Woosley S. E., 2002, *ApJ*, **567**, 532
- Kremer K., et al., 2020, *ApJ*, **903**, 45
- Leung S.-C., Nomoto K., Blinnikov S., 2019, *ApJ*, **887**, 72
- Lombardi James C. J., Rasio F. A., Shapiro S. L., 1996, *ApJ*, **468**, 797
- Lombardi James C. J., Warren J. S., Rasio F. A., Sills A., Warren A. R., 2002, *ApJ*, **568**, 939
- Lombardi J. C. J., Proulx Z. F., Dooley K. L., Theriault E. M., Ivanova N., Rasio F. A., 2006, *ApJ*, **640**, 441
- Mapelli M., et al., 2021, *MNRAS*, **505**, 339
- Mapelli M., Bouffanais Y., Santoliquido F., Arca Sedda M., Artale M. C., 2022, *MNRAS*, **511**, 5797
- Marchant P., Moriya T. J., 2020, *A&A*, **640**, L18
- Marchant P., Renzo M., Farmer R., Pappas K. M. W., Taam R. E., de Mink S. E., Kalogera V., 2019, *ApJ*, **882**, 36
- McKernan B., Ford K. E. S., Lyra W., Perets H. B., 2012, *MNRAS*, **425**, 460
- McKernan B., et al., 2018, *ApJ*, **866**, 66
- Miller M. C., Hamilton D. P., 2002, *MNRAS*, **330**, 232
- Nitz A. H., Kumar S., Wang Y.-F., Kastha S., Wu S., Schäfer M., Dhurkunde R., Capano C. D., 2021, arXiv e-prints, p. [arXiv:2112.06878](#)
- Paxton B., Bildsten L., Dotter A., Herwig F., Lesaffre P., Timmes F., 2011, *ApJS*, **192**, 3
- Paxton B., et al., 2019, *ApJS*, **243**, 10
- Price D. J., 2007, *Publ. Astron. Soc. Australia*, **24**, 159
- Rasio F. A., Shapiro S. L., 1995, *ApJ*, **438**, 887
- Rastello S., Mapelli M., Di Carlo U. N., Iorio G., Ballone A., Giacobbo N., Santoliquido F., Tornamenti S., 2021, *MNRAS*, **507**, 3612
- Renzo M., Farmer R. J., Justham S., de Mink S. E., Göteborg Y., Marchant P., 2020a, *MNRAS*, **493**, 4333
- Renzo M., Cantiello M., Metzger B. D., Jiang Y. F., 2020b, *ApJ*, **904**, L13
- Rodriguez C. L., Zevin M., Amaro-Seoane P., Chatterjee S., Kremer K., Rasio F. A., Ye C. S., 2019, *Phys. Rev. D*, **100**, 043027
- Rodriguez C. L., et al., 2020, *ApJ*, **896**, L10
- Schneider F. R. N., Ohlmann S. T., Podsiadlowski P., Röpké F. K., Balbus S. A., Pakmor R., Springel V., 2019, *Nature*, **574**, 211
- Sills A., Faber J. A., Lombardi James C. J., Rasio F. A., Warren A. R., 2001, *ApJ*, **548**, 323
- Spera M., Mapelli M., 2017, *MNRAS*, **470**, 4739
- Spera M., Mapelli M., Giacobbo N., Trani A. A., Bressan A., Costa G., 2019, *MNRAS*, **485**, 889
- Stevenson S., Sampson M., Powell J., Vigna-Gómez A., Neijssel C. J., Szécsi D., Mandel I., 2019, *ApJ*, **882**, 121
- Stone N. C., Metzger B. D., Haiman Z., 2017, *MNRAS*, **464**, 946
- Tagawa H., Haiman Z., Kocsis B., 2020, *ApJ*, **898**, 25
- Tagawa H., Kocsis B., Haiman Z., Bartos I., Omukai K., Samsing J., 2021, *ApJ*, **908**, 194
- Tanikawa A., Susa H., Yoshida T., Trani A. A., Kinugawa T., 2021, *ApJ*, **910**, 30
- Woosley S. E., 2017, *ApJ*, **836**, 244
- Woosley S. E., Heger A., 2021, *ApJ*, **912**, L31
- Woosley S. E., Blinnikov S., Heger A., 2007, *Nature*, **450**, 390
- Yang Y., Bartos I., Haiman Z., Kocsis B., Márka Z., Stone N. C., Márka S., 2019, *ApJ*, **876**, 122

This paper has been typeset from a \LaTeX file prepared by the author.